INSTITUTE OF PHYSICS PUBLISHING JOURNAL OF PHYSICS: CONDENSED MATTER

J. Phys.: Condens. Matter **18** (2006) S1703–S1719 doi:10.1088/0953-8984/18/32/S02

Unbalanced magnetic field configuration: plasma and film properties

S E Rodil and J J Olaya

Instituto de Investigaciones en Materiales, Universidad Nacional Autónoma de México, Circuito Exterior s/n, Ciudad Universitaria, 04510 México DF, Mexico

Received 11 October 2005
Published 24 July 2006
Online at stacks.iop.org/JPhysCM/18/S1703

Abstract

Coatings of CrN, TiN, ZrN, TaN and NbN were deposited using an unbalanced magnetron sputtering system with two different degrees of unbalancing to investigate the effect of the degree of unbalancing on both plasma characteristics and film properties. The degree of unbalancing was determined by an extensive characterization of the magnetic field fluxes in the X–Z plane perpendicular to the target. Then, the plasma parameters, such as electron temperature, plasma potential, plasma density and ion current density, were obtained for each target and as a function of the unbalance coefficient. The film microstructure, hardness, corrosion and wear resistant were measured to determine the effect of the degree of unbalancing on these properties. The results suggested that the degree of unbalancing, through the variations induced in the ion bombardment and plasma ionization, had a strong influence on the film hardness, microstructure and preferred orientation.

(Some figures in this article are in colour only in the electronic version)

1. Introduction

The commercial use of thin films has been growing at a surprising rate over the last decades in almost all industrial fields. The most widely used process for the physical vapour deposition of thin films is magnetron sputtering (MS). During the last 30–40 years the basics and important aspects of MS have been studied and, despite some limitations, the systems are used to deposit a wide range of industrially important coatings. Some of these limitations have been surpassed by the development of the unbalanced magnetron systems, as was first demonstrated by Windows and Saavides [1]. In a conventional or balance magnetron system the charged particles in the plasma, particularly the electrons, are confined by the magnetic field at the cathode surface, and very few electrons and ions reach the substrate. By modifying the magnetic field configuration, Windows and Saavides [1] proved that it is possible to maintain a high level of cathode sputtering while increasing the number of charged particles reaching the substrate. This increment in the charged to neutral species or ion to atom flux arrival ratio (J_i/J_a)

is a fundamental parameter defining the structure and many properties of the films [2–4]. The ion to atom flux arrival ratio depends, for a fixed substrate–target distance, pressure and power, on the level of unbalance of the magnetic field configuration [1]. Soon after, several authors demonstrated the advantage of using unbalanced magnetron sputtering over conventional systems. For example, Kelly and Arnell [5] were able to define a new structural-zone model (SZM) including the effect of J_i/J_a as a fundamental parameter controlling the microstructure of metallic films. Petrov *et al* [6] developed a model to explain the variations on the film microstructure and texture as a function of the ion energy and the ion–atom flux ratio. Similarly, Mayrhofer *et al* [7] established the effects of the ion energy and the ion–atom flux on the microstructure, hardness, residual stresses and thermal stability of CrN coatings. The unbalancing in those previous systems and, as a consequence, the larger J_i/J_a-values, were obtained either by adding Helmholtz coils to conventional magnetron sputtering systems (MAC) [6, 7] or designing new setups using permanent magnets on the cathode (UBM) [1]. The degree of unbalancing, K, can be defined as the ratio of the Z magnetic field components from the central to peripheral magnets on the target surface, where K equals unity for a perfect balanced magnetron [8].

$$K = \frac{\int B_{\text{central}}\, \mathrm{d}Z_{\text{central}}}{\int B_{\text{external}}\, \mathrm{d}Z_{\text{external}}}.$$

The ion–atom flux was shown to depend on the unbalance coefficient and therefore K provides a useful parameter to design and compare magnetic field configurations in UBM systems [8].

Nevertheless, we consider that there is still one important part of the research that has not been performed: determination of the effect of different magnetic field configurations (different degrees of unbalancing) on both plasma and film properties. In this work, we investigated different degrees of unbalancing, created by varying the relative vertical position between the magnet assembly and the target, derived a map of the magnetic field flux for the different magnets arrangements as a function of both the radial and axial distances and studied the effect on the properties of ceramic metal nitride films, and on the plasma parameters. The film properties investigated include not only microstructure and hardness but also corrosion and wear resistance.

2. Experimental details

2.1. Deposition system

The magnetron is a commercial variable unbalanced magnetron from the company Teer Coatings Limited. An schematic of the cathode assembly is shown in figure 1. Briefly, the configuration of the magnetic field above the target was formed by a magnetic system based on permanent magnets. The diameter of the central magnet is 12 mm; the external and internal diameters of the outer magnets are 80 and 70 mm, respectively, and the height is 20 mm for both internal and external magnets. The configuration of the magnetic field was modified by changing the distance between the magnet assembly and the target. This distance was varied by turning a millimetre screw, which leads to a continuum variation in the unbalance coefficient. The characterization of the plasma parameters was made as a function of the number of turns, N_V, which were then correlated to the unbalance coefficient. An increment in N_V corresponds to enlarging the distance between the magnet assembly and the target. The metal nitride films were deposited only on two different configurations that correspond to those with the strongest variation in the plasma properties.

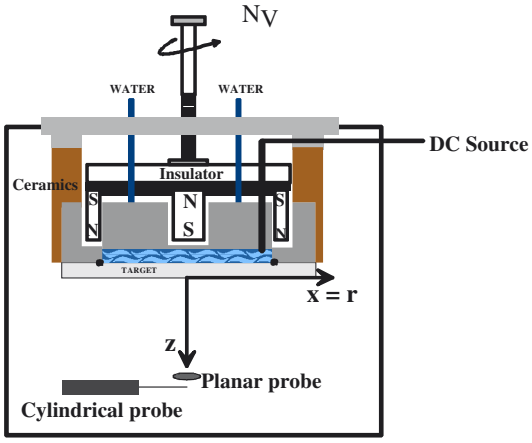

Figure 1. Schematic diagram of the variable unbalanced magnetron sputtering system and the position of the Langmuir probes.

2.2. Magnetic field and plasma characterization

The magnetic field was measured using a portable gaussmeter, Lakeshore Model 410, with a Hall-effect probe. Both components of the magnetic field, B_x and B_z, were measured as a function of Z (axial distance), r (radial distance), and N_V, as shown in figure 1. The sign convention proposed in figure 1 dictates that the B_x component is negative when directed toward the centre of the cathode, (0, 0) position, and vice versa. Similarly, the B_z component is negative when directed towards the target surface and positive when pointing out of it. Using this convention, the magnitude and direction of the magnetic field vectors were estimated using standard vector definitions.

The plasma parameters were determined using planar and cylindrical Langmuir probes; the position of the probes is shown in figure 1. The electron temperature, T_e, plasma density, n_e, and plasma potential, V_p, were calculated from the current–voltage characteristics [9] of the cylindrical probe (length 5.3 mm and radius 1.55 mm). The probe measurements were made in an argon plasma using the deposition parameters indicted in table 1 (pressure and power) for the different magnetic field configurations, at $Z = 5$ and $r = 0$ cm.

The planar probe (0.125 mm^2 area) was placed at the position of the substrate ($Z = 5$ cm), and electrically isolated from it. In this case, we use the N_2/Ar flow ratio as in the deposition conditions to determine the ion flux arriving at the substrate. For this, the probe was biased at -100 V to obtain the ion saturation current. Biasing is necessary to repel all the electrons from the plasma and obtain purely ionic currents in the electrometer [10]. Saturation currents were converted into ion current densities using the surface area of the probe and under the following assumptions: all ions are assumed to be singly charged [11] and no secondary electrons are emitted from the probe [10].

2.3. Film deposition

The coatings were deposited from high-purity targets 101 mm in diameter (Cr: 99.95%, Ti: 99.995%, Ta: 99.95% Nb: 99.95%, Zr: 99.2%), in Ar + N_2 (both of 99.99% purity) atmospheres. The base pressure in the chamber was less than 6×10^{-4} Pa. The deposition conditions for each film are listed in table 1; the values corresponding to pressure, flow-

Table 1. Deposition conditions; unbalance coefficient (K), power, pressure (P), argon flow-rate (Ar), nitrogen flow-rate (N_2) and homologous temperature (T_H = deposition temperature/melting temperature).

Sample	K	Power (W)	P (mTorr)	Ar (sccm)	N_2 (sccm)	T_H
NbN–0N_V	6.5	200	7	14	2	0.158
NbN–4N_V	8.1	200	7	14	2	0.158
TiN–0N_V	6.5	245	7	4.5	8.5	0.128
TiN–4N_V	8.1	245	7	4.5	8.5	0.128
CrN–0N_V	6.5	170	4	4.5	4.5	0.36
CrN–4N_V	8.1	170	4	4.5	4.5	0.36
ZrN–0N_V	6.5	130	7	14	2	0.127
ZrN–4N_V	8.1	130	7	14	2	0.127
TaN–0N_V	6.5	130	9	14	2	0.12
TaN–4N_V	8.1	130	9	14	2	0.12

rate and power were previously optimized to obtain a stoichiometric hard metal nitride. The substrate temperature was fixed at 380 °C, and the equivalent homologous temperature for each film is included in table 1. The deposition time was adjusted to set the thickness of all coatings about 1.8 μm and the substrate was grounded without any external bias. The coatings were simultaneously deposited onto various substrate materials chosen for their suitability for particular analysis techniques: samples deposited on silicon (111) were used for fracture cross-section views with scanning electron microscopy (SEM), residual stress and thickness determination with profilometry. Austenitic steel (AISI 304) was used for the x-ray diffraction (XRD) and x-ray photoelectron spectroscopy (XPS) studies and mechanical tests were done on coated tool steels (AISI M2). Prior to the metal nitride (MN_x) deposition a metal interlayer of 150 nm was deposited to improve the adhesion between the MN_x coating and the substrate.

2.4. Film characterization

The crystallographic phases of the coatings, texture and grain size were obtained by XRD analysis from the spectra taken using a Siemens D500 system in the Bragg–Brentano mode and Cu Kα radiation. The grain size was determined for the preferred orientations from calculations using the fit of the XRD peaks with a pseudo-Voigt function [12]. This method needs only a diffraction peak to obtain grain sizes and is based on the fact that the Lorentzian component of the experimental profile is due to crystalline size and that the Gaussian contribution arises from strain.

The surface chemical composition of the samples was obtained by XPS using a Thermo-Scientific Multilab ESCA 2000 with Mg Kα x-radiation (1253.6 eV) operating at 20 mA, with a 500 μm spatial resolution. These condition provide a full-width half maximum of 1 eV for the Ag $3d^{5/2}$ peak. The binding energy positions were calibrated using the previous silver peak at 367.7 eV and the C 1s peak at 284 eV, respectively. The N/metal ratios were obtained using the theoretical cross-section for the metal and N atoms given in the Scoffield data base [13].

The cross-sectional morphology of the films deposited onto Si(111) was studied using a Hitachi S-4700 Field Emission SEM. The sample thickness was measured using a stylus profilometry DEKTAK IIA by measuring the step left in a region that was masked prior to deposition. The microhardness of the films was determined using an ultra-microhardness tester MXTBO-UL with 0.25 N of load.

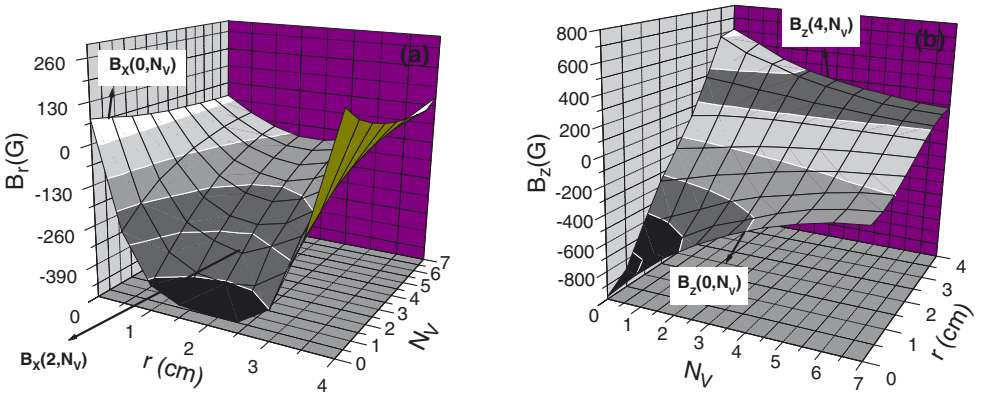

Figure 2. The magnetic field components at $Z = 0$ cm as a function of the radial distance from the target to the centre and the number of turns. The magnetic flux is given in Gauss. (a) $B_X(r, N_V)$ and (b) $B_Z(r, N_V)$.

The corrosion resistance was evaluated by electrochemical measurements. The potentiodynamic anodic polarization (PAP) studies were performed using a PCI4/300 Gamry potentiostat. The PAP tests were performed on all specimens, including the bare AISI 304 stainless steel substrate. The test set-up followed the American Society for Testing and Materials standard G5 [14]. The counter electrode was of graphite and the reference was a saturated calomel electrode (SCE). The electrolyte was 0.5 M H_2SO_4 containing 0.05 M KSCN; this electrolyte has been used quite extensively to determine the passivation currents and porosity in TiN and ZrN coatings [15–17]. Before the tests, the electrolyte solution was kept at room temperature for one hour. The sample was sealed to a wall of the electrochemical apparatus with a Viton O-ring leaving an area of 0.15 cm^2 exposed to the solution. The scans were conducted from -300 to 1000 mV at a scan rate of 20 mV min^{-1}.

The wear resistance of the films was evaluated using a ball cratering system, which is a microscale abrasion test. In this test, a hard steel sphere of $R = 30$ mm radius is rotated against a specimen in the presence of a slurry of fine abrasive particles (diamond suspension, 1/4 μm). The load used during the test was 2 N and the samples were evaluated at a speed of 100 rev min^{-1}, corresponding to a sliding distance of 47.5 m. The wear volume is then calculated by measurement of the crater dimensions and using the equation

$$V(\mathrm{mm}^3) = \frac{\pi b^4}{64R^2}\left(R - \frac{b^2}{8R}\right)$$

where b is the external diameter of the crater. The normalized wear coefficient k_{wear} is obtained by dividing the wear volume by the applied force and the sliding distance.

3. Results

3.1. Magnetic field configuration

Figure 2(a), (b) show each component of the magnetic field separately as a function of the number of turns and the radial distance at $Z = 0$ cm. From figure 2(a) it may be seen that the B_x component is positive but small at the centre and edge of the target and becomes more and more negative as X increases, attaining a minimum around 2 cm from the centre. This minimum (or maximum magnitude) around 2 cm was observed for all the magnetic field configurations

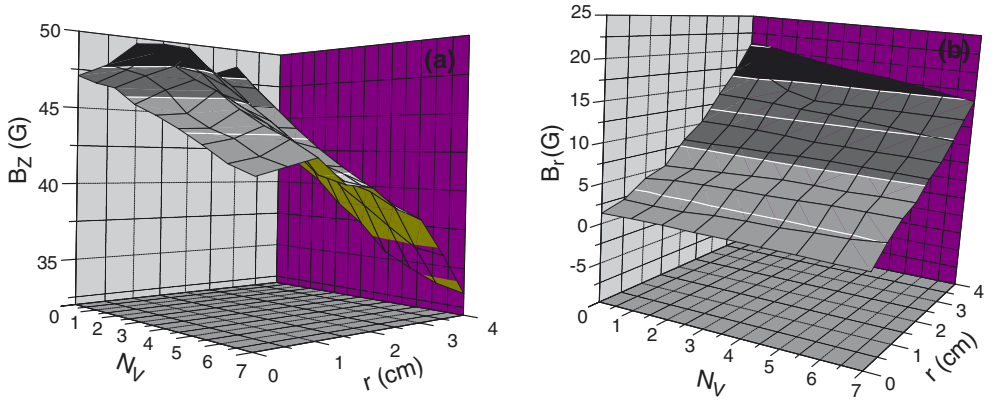

Figure 3. The magnetic field components at $Z = 5$ cm as a function of the radial distance from the target to the centre and the number of turns. The magnetic flux is given in Gauss. (a) $B_X(r, N_V)$ and (b) $B_Z(r, N_V)$.

(N_V). However, the absolute difference between the value at the centre of the target and at 2 cm $(|B_r(0, N_V) - B_r(2, N_V)|)$ decreased as N_V increased. The maximum magnitude was always observed at 2 cm from the centre and this distance corresponded exactly to the average radius of the maximum erosion depth-zone observed in the targets.

Figure 2(b) shows that B_Z changes direction as it moves out from the centre of the target. Near the centre $(r = 0)$, B_Z pointed to the target and, at the edge $(r = 4)$, it pointed out from it. A similar variation was observed for all the magnetic field configurations, but the magnitude variation $(|B_Z(0, N_V) - B_Z(4, N_V)|$ decreased as N_V increased, i.e., as the magnetic assembly moved away from the target. The combination of these different variations of the magnetic field components led to different degrees of unbalance as the number of turns increased.

Figures 3(a) and (b) show the magnetic field components, (a) B_x and (b) B_z, at the substrate position $(Z = 5, r = 0$ cm). B_z was uniform along the radial distance and its magnitude did not change significantly with the number of turns. B_x increased monotonically with the radial distance for all the magnetic field configurations, but its magnitude was rather low. This uniform field in the substrate region ensured a uniform ion bombardment and homogeneous film growth.

Figure 4 shows the total magnetic flux vectors (the magnitude of the vectors is in a logarithmic scale) for only two different magnetic configurations, corresponding to 0 and 4 turns. The position (Z_0) at which the magnetic field was zero (null-point, $\boldsymbol{B} = 0$) can be clearly observed for the two different magnetic field configurations. In both cases, it is also possible to appreciate that the field lines from the cathode periphery $(r > 3$ cm) were directed towards the substrate and did not formed a closed loop with the central magnet, as observed for conventional magnetrons. This is one of the essential differences between the unbalanced and balanced magnetron configurations. The Z_0-values obtained for the different magnetic configurations (N_V) are included in figure 4. As N_V increased Z_0 was closer to the target, i.e., the magnetron was more unbalanced.

The different values of the unbalance coefficient, K, as a function of the number of turns are shown in figure 5. According to the definition given by Svadlovski *et al* [8] all the magnetron configurations were unbalanced, but the degree or level of unbalancing increased as the N_V increased. In the following sections, the variation of plasma and the film properties are presented in terms of the unbalance coefficient K.

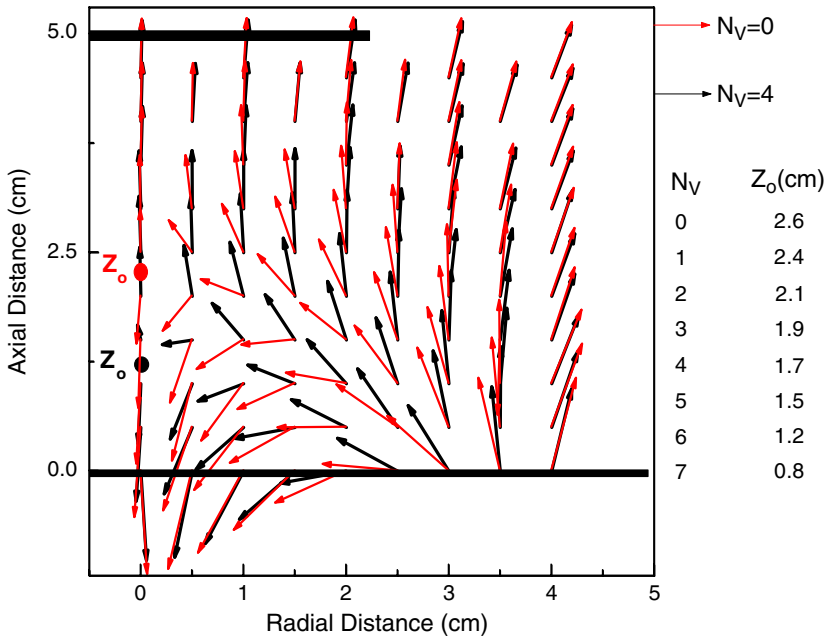

Figure 4. The magnetic field map $B(X, Z)$ for two K-values.

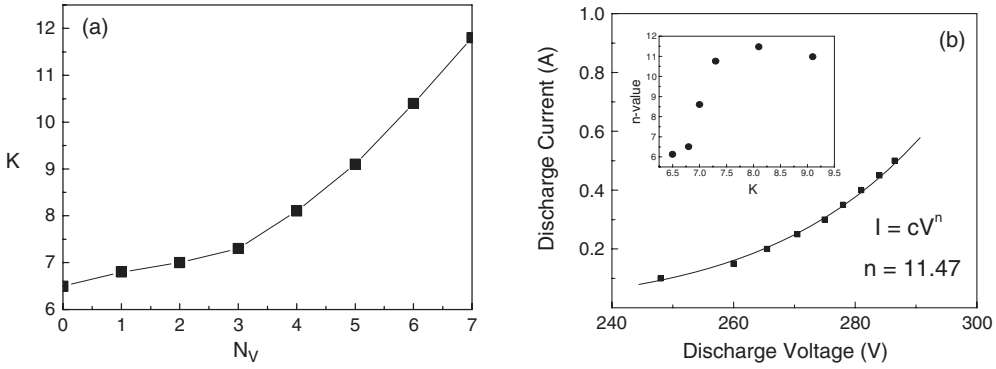

Figure 5. Unbalance coefficient as a function of the number of turns. (b) Current–voltage characteristic from which the n-value was determined for each K-value. The maximum n-value was 11.47, obtained using four turns. The inset shows the variation of the n-value versus K.

The optimum sputtering should occur when the B_x component is parallel to the target, which corresponds to the ring along the null-point; this will also correspond to the largest discharge current and highest sputtering rates. This situation cannot be easily observed in figures 2–4, therefore we decided to estimate the current–voltage characteristic of the magnetron to determine if there was a change in the magnetron efficiency with the unbalance coefficient. A sputtering system has a current–voltage (I–V) characteristic that behaves as $\boldsymbol{I = cV^n}$ (at constant pressure) [18]. The exponent n reflects how well the electrons are confined by the magnetic trap in the race track. An optimum magnetron should give an n-value which is typically around 5–9, and higher values indicated a better magnetic enhancement of the sputtering process. Figure 5(b) shows the current–voltage characteristic for an argon discharge

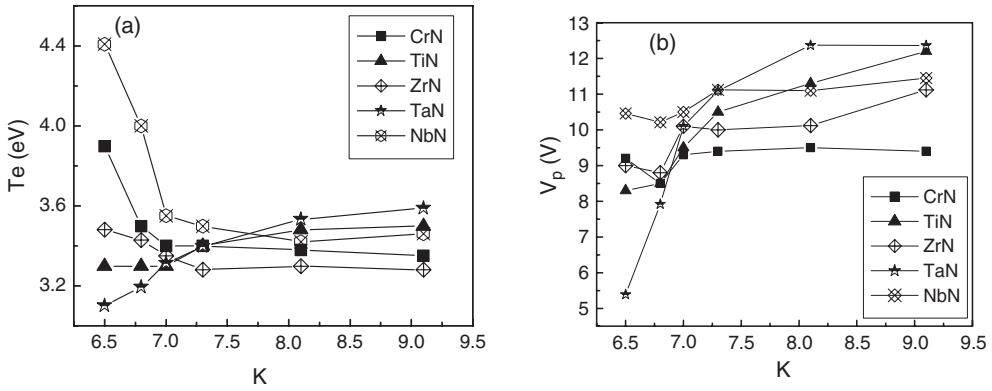

Figure 6. Plasma parameters calculated from the I–V curve of the cylindrical probe at $Z = 5$ cm. (a) Electron temperature as a function of the unbalance coefficient for each target material. (b) Plasma potential versus K for each material.

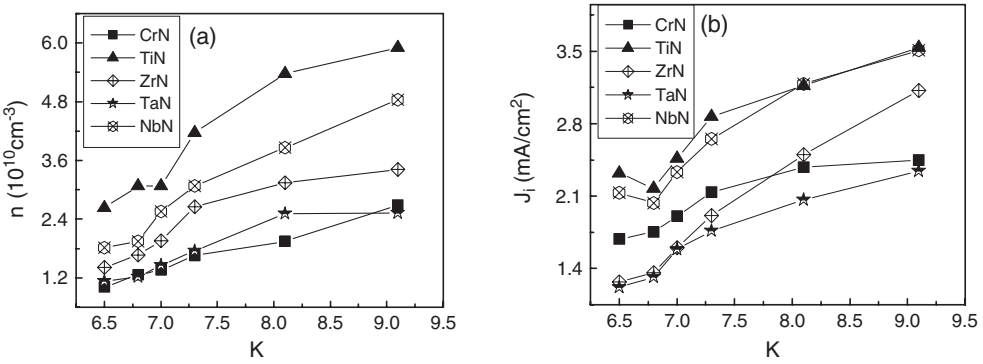

Figure 7. (a) Plasma density at $Z = 5$ cm estimated from the cylindrical probe for each target and as a function of K. (b) Ion current density measured using the planar probe situated at 5 cm from the target, for each material and as a function of K.

and using a Nb target, from which the n-values as a function of the unbalance coefficient K were calculated (inset in figure 5(b)). Figure 5(b) illustrates that the efficiency of the magnetron increased as the unbalance coefficient increased, although it was not a simple linear function and most probably the n-value was not the same for all target materials.

3.2. Plasma characterization

Figures 6(a) and (b) show the electron temperature and the plasma potential, respectively. It may be seen that both parameters (T_e and V_p) varied with K but the actual trend depended strongly on the cathode material. The strongest variations were observed for the Nb target, where T_e decreased abruptly for K larger than 7.5, while for the Ta target T_e increased monotonically. The plasma potential increased slightly for all samples, but the variation was stronger for Ta.

The plasma density as a function of K is shown in figure 7(a). It may be seen that the highest plasma density was obtained for Ti, attaining up to 6×10^{10} cm^{-3} for the more unbalanced configuration ($K = 9.1$). For all the magnetic configurations, the plasma density

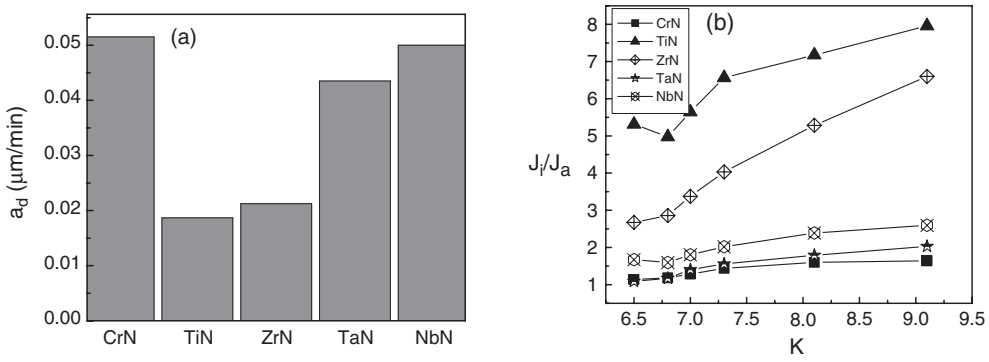

Figure 8. (a) Deposition rate of the different films measured at $K = 6.5$ and (b) ion-to-atom flux arrival ratios at the substrate position.

Table 2. The main results of the plasma characterization, which can affect the film properties: the unbalance coefficient, plasma potential, ion-to-atom flux ratio and the energy parameter.

Sample	K	V_p (V)	J_i/J_a	E_p (eV/atom)
NbN–0N_V	6.5	10.5	1.7	17.8
NbN–4N_V	8.1	11.1	2.4	26.7
TiN–0N_V	6.5	8.3	5.3	44
TiN–4N_V	8.1	11.3	7.2	81.4
CrN–0N_V	6.5	9.2	1.14	10.5
CrN–4N_V	8.1	9.5	1.6	15.2
ZrN–0N_V	6.5	9	2.7	24.3
ZrN–4N_V	8.1	10.1	5.3	53.6
TaN–0N_V	6.5	5.4	1.1	5.9
TaN–4N_V	8.1	12.4	1.8	22.3

increased as the unbalance coefficient increased. Similarly, the ion densities measured at the planar probe increased as the system became more unbalanced, as plotted in figure 7(b) for the five target materials.

In order to compare our results with those in which the ion–atom flux ratios, J_i/J_a have been measured, we estimated J_i/J_a for the different coatings and different K's. The deposition rate for each K-value was observed to be nearly constant, with a variation lower than 4% for any film. Similar results and explanations have been reported by Svadorski *et al* [8] showing that the deposition rate, at a fixed position, was practically independent of K and only depended on the discharge parameters. Therefore, we used the values represented in figure 8(a) to calculate the atom flux J_a,

$$J_a = \frac{a_d \rho}{M_v m_u}$$

where ρ is the film density (assumed as the density of the bulk stoichiometric compound), a_d is the deposition rate, M_v is the relative mass of the atoms conforming the film and m_u is the atomic mass (1.66×10^{-24} g uma^{-1}). Figure 8(b) shows the resulting ion–atom flux ratios as a function of K for all the samples. It may be seen that for the lower K-values (less unbalanced configuration) J_i/J_a was smaller and increased with the unbalance degree following different slopes for each material. The J_i/J_a-values were always above 1, which is also characteristic of unbalanced magnetron systems. A summary of the plasma properties is shown in table 2,

Table 3. Properties of the films deposited under two different unbalance coefficients.

Sample	K	N/M ratio	$f_{(200)}$	Grain size (nm)	Stress (GPa)	$HV_{0.025}$ (kg mm^{-2})	k_{wear} (mm^3 N m^{-1})	I_{corr} (μA cm^{-2})	E_{corr} (mV)	I_{crit} (mA cm^{-2})
Substrate	—		—			800	9.35×10^{-6}	31	−477	90.2
NbN–0N_V	6.5	1.05	0.99	$24.7_{(200)}$	−1.63	1812	3.85×10^{-6}	1.16	−350	0.16
NbN–4N_V	8.1	0.99	0.6	$34.8_{(111)}$	−2.49	2386	2.77×10^{-6}	2.7	−358	0.32
TiN–0N_V	6.5	0.9	1	$27.1_{(200)}$	−1.6	1625	7.01×10^{-6}	2.4	−370	0.23
TiN–4N_V	8.1	0.91	0.91	$17_{(200)}$	−1.69	1860	5.51×10^{-6}	2.5	−385	0.39
CrN–0N_V	6.5	1.08	1	$36.1_{(200)}$	−0.3	1564	9.25×10^{-6}	3.8	−353	0.18
CrN–4N_V	8.1	1.08	0.1	$42_{(111)}$	−1	2002	8.80×10^{-6}	4.1	−351	0.17
ZrN–0N_V	6.5	0.97	0.97	$23_{(200)}$	−2.18	2093	6.21×10^{-6}	0.3	−341	0.023
ZrN–4N_V	8.1	0.94	0.9	$17.4_{(200)}$	−2.52	2394	5.56×10^{-6}	1.7	−359	0.024
TaN–0N_V	6.5	—	0.9	$13.6_{(200)}$	−2.82	2115	3.18×10^{-6}	3.1	−355	0.097
TaN–4N_V	8.1	—	0	$29_{(111)}$	−4.01	2523	4.51×10^{-6}	4.1	−422	1.27

where we have also presented the energy parameter E_p defined as

$$E_p = E_i \times \frac{J_i}{J_a} \qquad E_i = e|V_p|.$$

3.3. Film properties

Table 3 shows the main film parameters estimated in this work. The composition was simply expressed as the nitrogen-to-metal ratio (N/M) and was estimated from the XPS spectra, except for the TaN films. In the case of TaN films, the estimation was not possible because the binding energy of the N 1s peak is very close to that of both Ta $4p^{3/2}$ and an Auger peak of Ta, making any N/Ta ratio estimation unreliable. It may be seen that the composition is not strongly affected by the magnetic field configuration and that, under the present deposition conditions, the films were nearly stoichiometric.

Figure 9 shows the XRD spectra of the metal nitride films deposited on AISI 304 for the two K-values. All films presented only a face-centred-cubic close-packed structure (fcc-NaCl); no other phases were observed, which was in good agreement with the composition results. However, the texture or preferred orientation was seen to change. The fraction of [200] orientation in the films was estimated from the normalized (200) XRD peak intensities $\boldsymbol{I}_{(200)}/(\boldsymbol{I}_{(200)} + \boldsymbol{I}_{(111)})$ and these texture coefficients are presented in table 3. The texture coefficient or index $f_{(200)}$ reflects how much of the film is oriented along the [200] direction, and values above 0.6 are a good indication of a preferred orientation [19]. Texture analysis using this simple technique, relative peak intensities in the XRD spectra, does not provide information about the distribution of crystals orientations in the materials, but strong variations in the texture index are a clear indication that substantial changes in film texture have taken place. The preferred orientation of NbN, CrN and TaN films changed from [200] to [111] as K increased, while the orientation for TiN and ZrN was preferentially [200] for the two magnetic field configurations. Figure 9 also shows strong variations in the XRD intensity of the main peaks, indicating differences in the sample crystallinity.

In general, it may be observed that the grain size and residual stresses increased with the degree of unbalancing, although for some films the variation was very small.

Figure 10 shows the different microstructures obtained for the coatings. Considering the size, morphology and orientation of the crystals, microstructures corresponding to zones T, 2

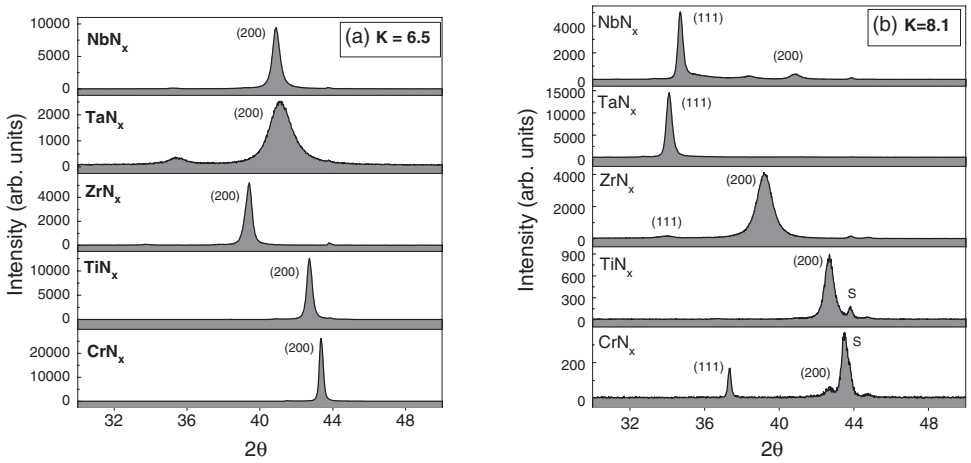

Figure 9. XRD spectra for the MN_x films deposited at two different unbalance coefficients (a) $K = 6.5$ and (b) $K = 8.5$.

and 3 of the structural zone models were distinguished. ZrN coatings deposited at the two K-values, TiN–$0N_V$ and CrN–$0N_V$ ($K = 6.5$), comprised a dense columnar and homogeneous microstructure, characteristic of zone 2. In classic SZMs [20, 21], the homologous temperature T_H at which zone-2 microstructure can be attained is higher than 0.4. The CrN coatings were deposited close to this value, but the TiN and ZrN films were deposited at T_H less than 0.2, suggesting the important role played by the high J_i/J_a ratios. For NbN–$4N_V$, TiN–$4N_V$ ($K = 8.1$) and both TaN coatings, the structure was inhomogeneous along the film thickness and the morphology was rougher than any other film, indicating a microstructure characteristic of zone T. Finally, the NbN–$0N_V$ ($K = 6.5$) and CrN–$4N_V$ ($K = 8.5$) coatings had a completely different microstructure that resemble more a globular profile, probably corresponding to zone 3. The fine topography of these films also suggested the formation of a zone-3 microstructure with equiaxed three-dimensional grains, even though the homologous temperature was not so high. These assignments were made taking into account the corrosion resistance results, as explained later.

The seventh column in table 3 shows the microhardness of the substrate–film system. Hardness measurements were made on samples deposited on the AISI M2 tool steel. The hardness of the substrate was 800 kg mm^{-2}. The hardness of the films was 2–3 times higher than the substrate hardness. Moreover, the data showed that the hardness increased as the degree of unbalance increased.

The wear coefficients were all in the 10^{-6} mm^3 N^{-1}m^{-1} range and the lower values were obtained for NbN and TaN films. It may be seen that there was a slight decrease in k_{wear} as the unbalance coefficient increased, but the variation was too small to be considered as important.

Figure 11 shows the potentiodynamic polarization curves for the ZrN_x films deposited at the two magnetic field configurations and the AISI 304 substrate, as an example. The corrosion resistance of a material in the polarization curve is determined by its ability to retain low current densities as the electric potential increases. Quantitatively, the Tafel analysis was used to determine the corrosion potential, E_{corr}, and the corrosion current density, I_{corr} [22], while the critical passivation current density, I_{crit}, was estimated from the maximum anodic dissolution current before passivation, as shown in figure 11 [16, 17]. The values of these parameters for the different coatings and the bare substrate are presented in the last columns of the table 3.

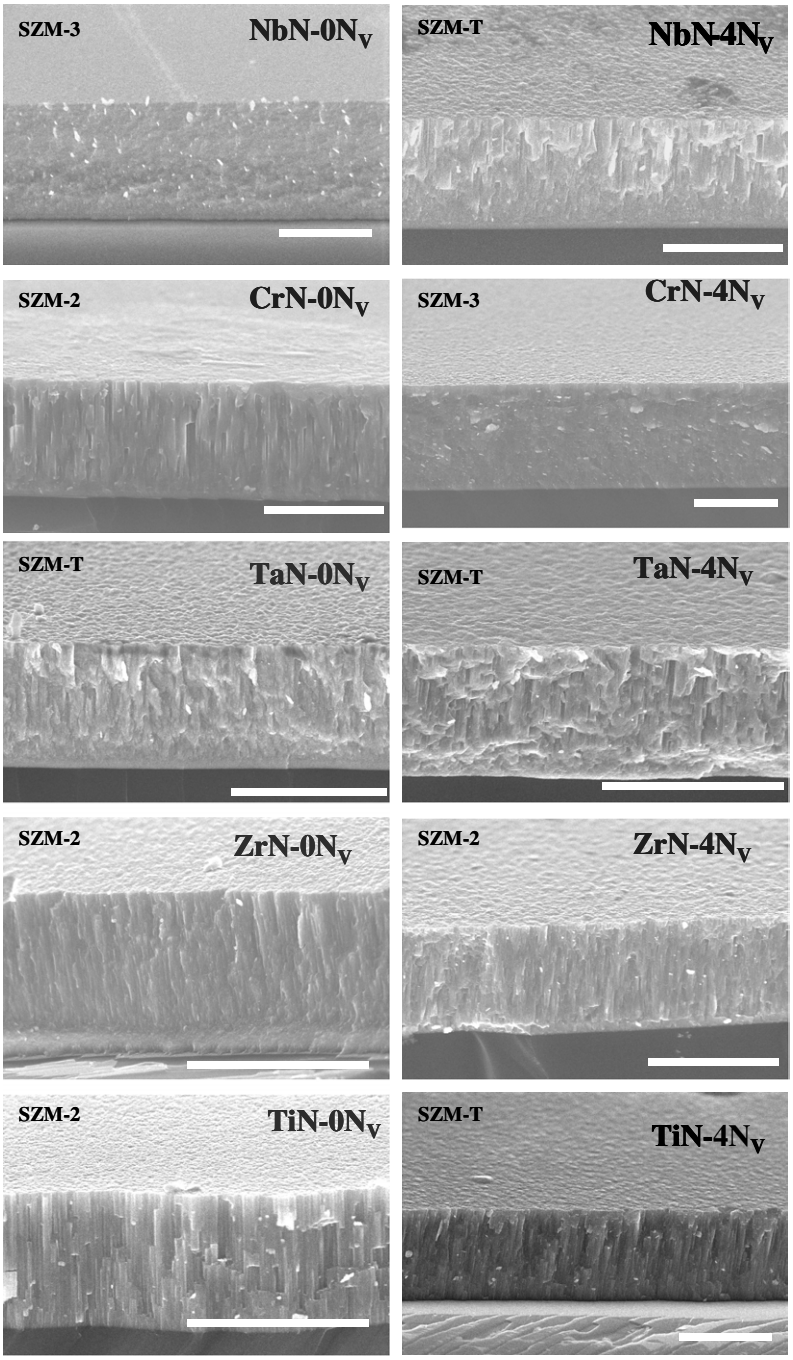

Figure 10. SEM cross-sectional images of the metal nitride samples deposited on silicon (111) substrates for each value of K. The scale bar is 2 μm.

The good corrosion resistance of the coatings can be seen from the more positive corrosion potential, the lower corrosion currents attaining values up to two orders of magnitude lower than the substrate, and the lower passivation currents relative to the substrate.

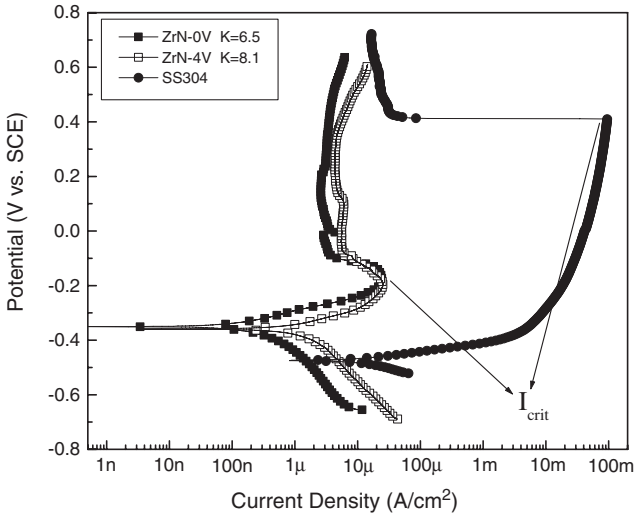

Figure 11. Polarization scans of the ZrN-coated AISI 304 substrates.

4. Discussion

Films of CrN, TiN, ZrN, TaN and NbN were deposited using an unbalanced magnetron sputtering system with different degrees of unbalancing to investigate its effect on both plasma characteristics and film properties. Initially, we obtained the magnetic field maps for the different unbalance coefficients. Then, the plasma parameters, such as electron temperature, plasma potential, plasma density and ion current density, were obtained for each target and as a function of the unbalance coefficient. The film microstructure, hardness, corrosion and wear resistant were measured to determine the effect of the degree of unbalancing on these properties.

Figures 2–4 gave an insight into the magnetic field map corresponding to a type-II unbalanced magnetron system designed using an arrangement of permanent magnets, in which the degree of unbalancing can be modified. Specifically, figure 3 showed that the magnitude of magnetic field flux, $\boldsymbol{B}$, decreased along the Z-axis and became zero at the null-point. The magnetic field flux increased thereafter but the increment was not substantial. The magnitude of $\boldsymbol{B}$ remained between 40 and 50 G to a distance of 5 cm for all values of K, while at the target position $\boldsymbol{B}$ decreased from 980 to 200 G when K increased from 6.5 to 11.8. These variations in the magnetic fluxes, very strong at the target position and moderate in the substrate region, are characteristics of UBM sputtering systems and lead to increments in both the ion fluxes and the plasma potential as the degree of unbalancing increases [23, 24]. This is very relevant, since the plasma potential corresponds to the energy at which ions reach a grounded substrate and this value is more significant at higher ion fluxes. Therefore, the lower the K, the lower the ion bombardment, as shown in table 2. For each film, there was an increment in the degree of ion bombardment with K. However, the increments were not the same for all films: for Ta the energy per condensing atom increased by a factor of $\sim$4, for Zr and Ti there was only a factor of $\sim$2, and for Nb and Cr a factor of $\sim$1.5.

The results obtained from the magnetic field distribution as a function of the radial and axial distances at different unbalance coefficients allowed us to note a relevant difference in the process by which UBM and MAC sputtering systems increase the J_i/J_a ratio at the substrate

position. By comparison of our results with those of Ivanov *et al* [25] and Petrov *et al* [26] that determined the magnetic field maps of unbalanced magnetrons assisted with external coils, some differences may be observed. They [25, 26] showed that the magnetic field fluxes close to the target were not affected by the coil current, while strong variations were observed near the substrate position. On the other hand, our results and those of Komath *et al* [23], suggested that in the UBM sputtering systems the stronger variations of the magnetic fluxes occur near the target. The different magnetic field configuration between the two systems indicated that the mechanism of enhanced ion bombardment at the substrate is not the same for MAC and UBM sputtering systems. In the MAC sputtering, most probably the increment in the ion–atom flux (J_i/J_a) is due to a major confinement of the discharge to the centre axis along Z and then the plasma is steered to the substrate, while in the UBM sputtering systems, the J_i/J_a increment might be due to an enhanced ionization close to the target. It is well known that the ionization processes close to the target are determined primarily by the radial component of the magnetic field, which bends the trajectories of the secondary electrons [27]. In our results, strong variations in the B_r component near the target were observed; therefore the ionization process must be affected. The enhanced ionization process was also suggested by the higher n-values shown in figure 5(b). In addition, the magnetic field lines from the external pole that were directed towards the substrate allowed the plasma to flow out, increasing further the plasma density and ion flux in the substrate region. The higher ionization of the Ar/N_2 plasma could explain the texture coefficient change observed for the TaN films, as will be explained shortly.

The different metal nitrides could not be deposited under exactly the same deposition conditions, such as nitrogen partial pressure and power, because at first, we searched for the conditions that produce nearly stoichiometric films. The formation of stoichiometric nitrides is known to be dependent on many parameters, including the nitrogen partial pressure [28], reactivity of the metal to nitrogen [29] or the heat of formation of the nitride [30]. Nevertheless, for each type of nitride the deposition conditions remained fixed when the magnetic field configuration was modified and in all cases it was possible to obtain nearly stoichiometric metal nitrides.

The increase in K and thus in the ion bombardment had a significant effect on the microstructure of the films, particularly the texture index, grain size and crystallinity. The strongest variations in V_p, J_i/J_a and E_p as K increased were obtained during the deposition of the ZrN and TiN coatings. The preferred orientation for those films was [200] in the two magnetic configurations, while for the other films a transformation from [200] to [111] was observed. The microstructure was dense-columnar in all cases, and some differences were observed as K varied in both the compactness and roughness. The relatively high J_i/J_a used to deposit the films allowed us to obtain typical microstructures of zone T, 2 and 3, even at homologous temperatures below the defined limits in the SZMs [20, 21]. The mechanism by which the ion bombardment promoted dense microstructures was basically by enhancing the adatom mobility and diffusitivity through direct kinetic energy transfer from the arriving ions to the adatoms, which was also reflected in the growth of the grains as K increased [31, 32]. The crystalline orientation, on the other hand, is a more complex parameter that results from a competitive process involving the diffusivity of the metal atoms, the surface energy of the different crystalline planes, the growth rate on each crystalline orientation and the creation and chemisorption of atomic nitrogen at the surface [6, 33, 34]. Petrov *et al* [6] explained the texture evolution and microstructure formation of polycrystalline thin films taking into account the effects of ion energy, ion flux and the presence of atomic nitrogen. In that paper [6], they reported that the texture of TaN deposited at ion energies below 20 eV and J_i/J_a less than 6.3 was preferentially [111] and only when J_i/J_a and/or the ion energy were higher could

the texture change to [200]. The reason given was that incident N_2 ions having energies >20 eV suffered collisional dissociation providing a continuous source of atomic nitrogen which chemisorbed in the 001 grains and captured Ta adatoms, resulting in the development of the [200] texture. Analysing our data for the TaN films, neither the ion energy nor the J_i/J_a ratios were in the range presented by Petrov *et al* [6]. Nevertheless, in our work, a complete 200 texture was obtained at a J_i/J_a ratio of 1.1 and ion energy around 5 eV, a result that, following Petrov's model, might be explained by a more efficient ionization and dissociation of the N_2 molecules in the plasma, as suggested also by our results of the plasma characterization. Other authors have also observed that both parameters (E_i and J_i/J_a) need to be higher than a critical value to obtain a pronounced [111] orientation in TiN films [35, 7], while Petrov *et al* [6] showed an opposite response; TiN films presented a change in texture from [111] to [200] with increasing E_i above 800 eV at very low $J_i/J_a<1$. Possible explanations for these discrepancies may be the difference in the N_2 ionization and dissociation of the plasmas or the effect of the substrate orientation on the film texture, ion incidence angle, or N_2 flux [33, 36, 37].

The microhardness for all the ceramic films was higher than for the substrate and the values followed the expected order considering the family of metal nitrides to which they correspond [38]. The group-IV nitrides generally are harder than those of group V [39]. The microhardness increased with the unbalance coefficient and so did the residual compressive stress for all films, a relation that has been extensively reported [40]. Moreover, the harder films were those having the preferred [111] orientation. Despite this increment of the film hardness, the abrasive wear coefficient against the stainless steel ball was not significantly improved when compared to the value obtained for the substrate. In addition, no clear trend was observed as the unbalance coefficient was increased. It might be a consequence of variations in other film properties, such as the coefficient of friction or the roughness, parameters known to exert an strong influence on the wear performance of the surfaces [41].

Regarding the corrosion resistance, we observed that all the films had lower corrosion rates (I_{corr}) than the AISI 304 stainless steel substrate and similarly, the corrosion potentials were more positive, indicating a more passive material. However, in contrast to the other film properties, there was a decrement in the corrosion resistance of the films as the unbalance coefficient increased. The rise in the corrosion current with K was very small for the NbN and TiN films, but significantly higher for TaN, ZrN and CrN. Probably, the higher ion bombardment induced by the degree of unbalancing created more defects, increasing the residual stresses and therefore deteriorating the film–substrate adhesion and consequently the response of the coatings to the corrosion products, as was visually observed at the end of the corrosion test for the TaN–4N_V film.

Similarly, the critical passivation current density, I_{crit}, increased with K. The critical passivation current density is proportional to the exposed area of the substrate due to the existence of pores or pinholes in the film [42]. Therefore, the results reported in table 3 suggested that as the unbalance coefficient increased there was more substrate area exposed at the bottom of the pinholes. These pinholes or defects are usually localized at the grain boundaries, which are defined by the crystal growth process, which consequently models the final film structure [43]. Thus, the combined analysis of the corrosion resistance and the SEM images might be used to properly define the microstructure type of the film within the SZMs. The lower I_{crit} must correspond to films having a more dense structure and this information was used to assign the film microstructures shown in figure 10.

5. Conclusions

This study investigated the influence of the degree of unbalancing on the magnetic field fluxes, as well as on the plasma and film properties. The films were five different metal nitrides, CrN,

NbN, TaN, TiN and ZrN, which were deposited under two dissimilar degrees of unbalancing ($K = 6.1$ and 8.5). Film composition, microstructure, hardness, wear and corrosion resistance were studied. The results suggested that the degree of unbalancing is another dimensional parameter, like pressure or power, that could be used to modify the film texture, structure, morphology, as well as mechanical and resistance corrosion properties. By modifying the unbalance coefficient, K, it was possible to finely adjust the energy and the ion–atom flux ratio incident at the substrate. The possibility of modifying the ion bombardment parameters (E_i and J_i/J_a) during deposition, maintaining constant erosion rates, has important implications for the development of industrial coatings.

The optimum degree of unbalancing, however, is not a universal parameter. The optimum value depends on the film properties that are more important for the proposed application: for example, hardness or chemical resistance. The corrosion resistance was reduced at higher values of K probably due to the formation of high residual stress and defects at the coating with excessive bombarding. The optimum value was also different among the nitrides. High K-values were good enough to obtain a preferred [111] orientation in NbN and TaN films, but not sufficient for TiN and ZrN. Similarly, the microstructure was not necessarily improved at high K-values for all films.

One correlation appears to exist between the effect of the unbalance coefficient and the type of nitride: group-IV nitrides (TiN and ZrN) had a similar response, which was different to that of group-V (Ta and Nb) and group-VI nitrides (CrN). This correlation might be determined by the known differences among the properties of refractory nitrides, such as the heat of formation (which is higher for group-IV nitrides), the more ionic character of the metal–nitrogen bond in group-IV nitrides, and the differences in the N/metal atomic ratio. However, more extensive studies are necessary to demonstrate this preliminary conclusion.

On the other hand, the magnetic flux characterization and plasma parameters determined as a function of the unbalance coefficient suggested that the enhancement of the ion–atom flux ratio in the substrate region was a consequence of both a higher ionization of the plasma at the target surface and the increased flow of the plasma to the substrate guided by the external pole magnetic lines.

Acknowledgments

The SEM analysis was carried out in the Center for Microanalysis of Materials, University of Illinois, which is partially supported by the US Department of Energy under grant DEFG02-91-ER45439. SER and JJO thanks L Huerta for XPS measurements. The authors would also like to acknowledge the financial support given to this project by DGAPA (Projects IN100701, IN100203) and CONACYT (Projects I36965-N, J200.730). JJO expresses his thanks to the SRE-CONACYT for his PhD scholarship.

References

[1] Window B and Savvides N 1986 *J. Vac. Sci. Technol.* A **4** 196
[2] Mitterer C, Mayrhofer P H, Waldhauser W, Kelesoglu E and Losbichler P 1998 *Surf. Coat. Technol.* **108/109** 230
[3] Kelly P J and Arnell R D 1998 *Surf. Coat. Technol.* **109** 317
[4] Ensinger W 1997 *Nucl. Instrum. Methods Phys. Res.* B **127/128** 796
[5] Kelly P J and Arnell R D 1998 *J. Vac. Sci. Technol.* A **16** 2858
[6] Petrov I, Barne P B, Hultman L and Greene J E 2003 *J. Vac. Sci. Technol.* A **21** S117
[7] Mayrhofer P H, Kunc F, Musil J and Mitterer C 2002 *Thin Solid Films* **415** 151
Mayrhofer P H, Tischler C and Mitterer C 2001 *Surf. Coat. Technol.* **142–144** 78
[8] Svadlovski I V, Golosov D A and Zavatskiy S M 2003 *Vacuum* **68** 283

[9] Camps E, Ordaza R and Anguiano G 1992 *Rev. Mex. Fis.* **38** 825
[10] Lochte-Holtgreven W 1995 *Plasma Diagnostic* (New York: American Vacuum Society Classics)
[11] Petrov I, Myers A, Greene J E and Abelson J R 1994 *J. Vac. Sci. Technol.* A **12** 2846
[12] De Keijser Th H, Langford J I, Mittemeijer E J and Vogels A B 1982 *J. Appl. Crystallogr.* **15** 308
[13] Scoffield J H 1973 Theoretical Photoionization cross sections from 1 to 1500 keV *Lawrence Livermore National Laboratory Rep.* UCRL-51326
[14] ASTM G5-4 2000 Standard reference test method for making potentiostatic and potentiodynamic anodic polarization measurements 2000 *Annual Book of ASTM Standards* vol 3, p 57 (Wear and Erosion; Metal Corrosion)
[15] Fukai T 1992 *Corros. Eng.* **41** 903
[16] Okamato T, Fukushima M and Takizawa K 1996 *Corros. Eng.* **45** 425
[17] Chou W J, Yu G P and Huang J H 2003 *Surf. Coat. Technol.* **167** 59
[18] Rossnagel S M and Kaufman H R 1988 *J. Vac. Sci. Technol.* A **6** 223
[19] Chen Y M, Yu G P and Huang J H 2001 *Surf. Coat. Technol.* **141** 156
[20] Thornton J A 1971 *Annu. Rev. Mater. Sci.* **7** 239
[21] Messier R, Giri A P and Roy A R 1984 *J. Vac. Sci. Technol.* A **2** 500
[22] Stansbury E E and Buchnan R A 2000 *Fundamentals of Electrochemical Corrosion* (USA: ASM International)
[23] Komath M, Mohan Rao G and Mohan S 1999 *Vacuum* **52** 307
[24] Groudeva-Zotova S 1998 *Surf. Coat. Technol.* **100/101** 300
[25] Ivanov I, Kasansky P, Hultman L, Petrov I and Sundgren J E 1994 *J. Vac. Sci. Technol.* A **12** 314
[26] Petrov I, Ivanov I and Orlinov V 1993 *J. Vac. Sci. Technol.* A **11** 2733
[27] Penfold A S 1995 Magnetron sputtering *Handbook of Thin Film Process Technology* p A3:2:1
[28] Wang S H, Chang C C and Chen J S 2004 *J. Vac. Sci. Technol.* A **22** 2661
[29] Hofmann S 1990 *Thin Solid Films* **191** 335
[30] Mientus R and Ellmer K 1999 *Surf. Coat. Technol.* **116–119** 1093
[31] Banerjee R, Chandra R and Ayyub P 2002 *Thin Solid Films* **405** 64
[32] Patsalas P, Charitidis C and Logothetidis S 2000 *Surf. Coat. Technol.* **125** 335
[33] Ma C H, Huang J H and Chen H 2004 *Thin Solid Films* **446** 184
[34] Schell N, Petersen JH, Bøttiger J, Mücklich A, Chevallier J, Andreasen K P and Eichhorn F 2003 *Thin Solid Films* **426** 100
[35] Zlatanović M, Beloševac R, Popović N and Kunosić A 1998 *Surf. Coat. Technol.* **106** 150
[36] Guruvenket S and Mohan Rao G 2002 *J. Vac. Sci. Technol.* A **20** 678
[37] Liu C P and Yang H G 2003 *Thin Solid Films* **444** 111
[38] Sundgren J E and Hentzell H T G 1986 *J. Vac. Sci. Technol.* A **4** 2259
[39] Holleck H 1986 *J. Vac. Sci. Technol.* A **4** 2661
[40] Cunha L, Andritschky M, Pischow K and Wang Z 1999 *Thin Solid Films* **355/356** 465
[41] Hsu S M and Shen M 2004 *Wear* **256** 867
[42] Uchida H, Inoue S and Koterazawa K 1997 *Mater. Sci. Eng.* A **234–236** 649
[43] Barna P B and Adamik M 1998 *Thin Solid Films* **317** 27